metals

Article

Effect of Prolonged Austempering Within Transformation Stasis on the Microstructural Evolution and Mechanical Behavior of Nanostructured Bainitic Steel

Xubiao Wang [1], Yanhui Wang [2,*], Dongyun Sun [3], Jun Cheng [4], Lin Wang [5], Wei Liu [1,5], Cheng Liu [1,5], Zhinan Yang [3,*], Fucheng Zhang [3] and Wanshuo Sun [6]

1 Xi'an QinChuang High Purity New Materials Technology Co., Ltd., Xi'an 710016, China; wxb19921202@163.com (X.W.); liuwei2017100214@163.com (W.L.); zzuliucheng@126.com (C.L.)
2 Key Laboratory of Intelligent Industrial Equipment Technology of Hebei Province, Hebei University of Engineering, Handan 056038, China
3 Hebei Iron and Steel Laboratory, North China University of Science and Technology, Tangshan 063210, China; dongyunsun93@163.com (D.S.); zfc@ysu.edu.cn (F.Z.)
4 Shaanxi Key Laboratory of Biomedical Metal Materials, Northwest Institute for Nonferrous Metal Research, Xi'an 710016, China; chengjun_851118@126.com
5 National Technology Innovation Center for Advanced Rare Metal Materials, Xi'an 710100, China; wlin0209@163.com
6 Institute of Electrical Engineering, Chinese Academy of Sciences, Beijing 100190, China; sun-wanshuo@mail.iee.ac.cn
* Correspondence: wangyanhui@hebeu.edu.cn (Y.W.); zny@ncst.edu.cn (Z.Y.)

Abstract

This study examines the evolution of microstructure, the metastability of retained austenite (RA), and the corresponding mechanical behavior exhibited by a nanostructured bainitic bearing steel subjected to prolonged austempering within a transformation stasis regime. The results indicate that following the completion of nanostructured bainitic formation at 300 °C for 3 h, a prolonged austempering time does not alter the microstructure, but reduces the dislocation density in BF while increasing the carbon content in RA. For the 4 h and 6 h specimens, a reduction in the overall RA mechanical stability is observed, accompanied by different transformation rates of stress-induced martensite during tensile deformation. This behavior is largely due to the weakened constraint effect of the BF matrix and the evolution of a carbon concentration gradient within the RA. During the transformation stasis, prolonged austempering elevates the yield strength while maintaining an unchanged ultimate tensile strength, albeit with a marginal reduction in microhardness. Relative to the baseline elongation recorded for the 3 h specimen, both the 4 h and 6 h specimens exhibit enhanced ductility, with the 4 h specimen yielding a peak value of 16.8%, which is 1.66 times that of the 3 h specimen. This improvement stems largely from the greater RA volume fraction that transforms into stress-induced martensite in the 4 h specimen, as well as its continuous and stable transformation rate during tensile deformation. Therefore, it can be concluded that an appropriately prolonged austempering time within nanostructured bainitic transformation stasis is essential for optimizing mechanical performance. This study provides a low-cost, energy-saving isothermal heat treatment technical scheme for mass industrial production of high-performance bearing steel.

Keywords: nanostructured bainitic steel; austempering; transformation stasis; retained austenite; mechanical properties

Check for updates

Academic Editor: Andrii Kostryzhev

Received: 14 July 2026
Revised: 10 August 2026
Accepted: 11 August 2026
Published: 13 August 2026

Copyright: © 2026 by the authors. Licensee MDPI, Basel, Switzerland. This article is an open access article distributed under the terms and conditions of the Creative Commons Attribution (CC BY) license.

1. Introduction

Ferrite laths in the nanostructured bainitic microstructure have been refined to the nanometer scale, at which the tensile strength has been reported to reach 2300–2500 MPa, and the maximum hardness can exceed 700 HV. Meanwhile, theinterlath RA exhibits the TRIP effect, thereby increasing work-hardening capability and impeding crack growth [1–3]. These factors result in an exceptional combination of toughness and strength in nanostructured bainitic steels, as well as superior wear and fatigue resistance. Consequently, nanostructured bainitic steels are extensively utilized in automotive sheets, rails, crankshafts, gears, and bearings [4–6].

To obtain nanostructured bainitic steel, the alloy composition is designed to achieve a low martensite start temperature, followed by austempering at a relatively low temperature [7–9]. As austempering time increases, the BF volume fraction rises gradually. During the phase transformation, carbon partitioning from BF into adjacent undercooled austenite intensifies, thereby enhancing the chemical stability of the latter [10–12]. The bainitic transformation completes once the undercooled austenite attains the carbon content prescribed by the T_0' curve [13]. This is known as the incomplete transformation phenomenon of bainite, where the austenite cannot fully transform into bainite, resulting in a certain amount of RA.

Due to the high silicon content in nanostructured bainitic steels, carbide precipitation is suppressed [14–16]. After the nanostructured bainitic transformation completes, no significant changes in the microstructure, phase fraction, or phase size are observed with further prolongation of the austempering time [17]. However, studies have shown that once the nanostructured bainitic transformation has completed, further increasing the austempering time promotes the uphill migration of carbon atoms from BF to RA. This process further enriches RA with carbon atoms and homogenizes their distribution within it. The mechanical stability of RA in nanostructured bainitic steels increases with its carbon content, thereby affecting their mechanical properties [18–20]. For instance, Zhao et al. reported that prolonged austempering time within transformation stasis led to a significant increase in elongation without a substantial decrease in strength [21]. However, this treatment was found to be detrimental to the low-cycle fatigue performance, which was primarily attributed to the homogenization of carbon within RA. Hofer et al. reported that the fractions of BF and RA remained essentially unchanged when austempering was prolonged within the transformation stasis regime [22]. Nevertheless, the gradual spheroidization of film-like RA brought about a considerable rise in both work-hardening capacity and elongation. Shakeri et al. found that prolonging the austempering time within transformation stasis significantly enhanced the strength and elongation [23]. Therefore, one can conclude that prolonging the austempering time within the transformation stasis period provides a viable way to tune the full set of mechanical properties in nanostructured bainitic steels.

Although the mechanical stability of RA is primarily governed by its carbon content [24–26], previous detailed investigations on tempered GCr15SiMo nanostructured bainitic steel have shown that, after tempering, this stability decreases with increasing carbon content [27]. A major factor behind this phenomenon is the weaker shielding provided by BF to RA. Compared with traditional studies mainly focusing on bainite transformation kinetics and short-time isothermal processes, this work provides a more in-depth investigation into the evolution of retained austenite and mechanical properties during prolonged isothermal holding, which has rarely been systematically discussed in the existing literature. Unlike previous qualitative analyses, this study quantitatively reveals the carbon homogenization behavior and dislocation density evolution, and clarifies the competitive mechanism between carbon partitioning and dislocation recovery. Such

comprehensive quantitative analysis and mechanism interpretation offer a more explicit theoretical basis for optimizing heat treatment processes for high-strength bainitic steels.

Hence, this work aims to further examine the microstructural evolution, the mechanical stability of RA, and the resulting mechanical properties of GCr15Si1Mo steel as a function of austempering time within the transformation stasis regime. Specifically, it aims to elucidate how the stability of RA is influenced by factors such as the strength of BF laths and the carbon content of RA, among others. This investigation will subsequently enrich and refine the theories concerning the mechanical stability of RA in GCr15Si1Mo bearing steel, as well as optimize the associated mechanical property parameters. Furthermore, it will clarify the dual competitive effect of bainitic ferrite dislocation recovery and carbon homogenization on mechanical performance, which enriches the fundamental theory of carbide-free nanostructured bainitic bearing steel.

2. Materials and Methods

The overall experimental framework and additional details are summarized in Appendix A. The investigated steel, with a nominal composition of Fe-0.97 C-1.24 Si-0.37 Mn-1.58 Cr-0.34 Mo (wt.%), was vacuum-induction-cast into an ingot, homogenized at 1250 °C for 10 h, and finally hot-forged. Using a DIL805A/D dilatometer (TA Instruments, Hüllhorst, Germany), the bainitic transformation kinetics curve for the present steel was obtained. The specimen was austenitized at 1050 °C and austempered at 300 °C (Figure 1a). An incubation period of 30 min was identified for the bainitic transformation. The bainitic transformation rate approached zero after austempering at 300 °C for 3 h, as shown in Figure 1b, indicating that the transformation is essentially complete. As shown in Figure 1c, the steel was austenitized at 1050 °C for 0.5 h, cooled to approximately 950 °C, and then immediately transferred into a salt bath furnace held at 300 °C. Direct quenching from 1050 °C to 300 °C in a salt bath allows for an ultra-fast cooling rate, which generates severe thermal stress and easily induces quenching cracks. Cooling slowly to 950 °C with controlled furnace cooling enables moderate grain boundary relaxation, avoiding abnormal austenite grain coarsening at high temperature. Temperature homogenization at 950 °C reduces the temperature difference between specimen surface and core before salt bath transfer. Three austempering durations were applied: 3 h, 4 h, and 6 h. The resulting specimens were designated according to their holding time, i.e., the 3 h, 4 h, and 6 h specimens.

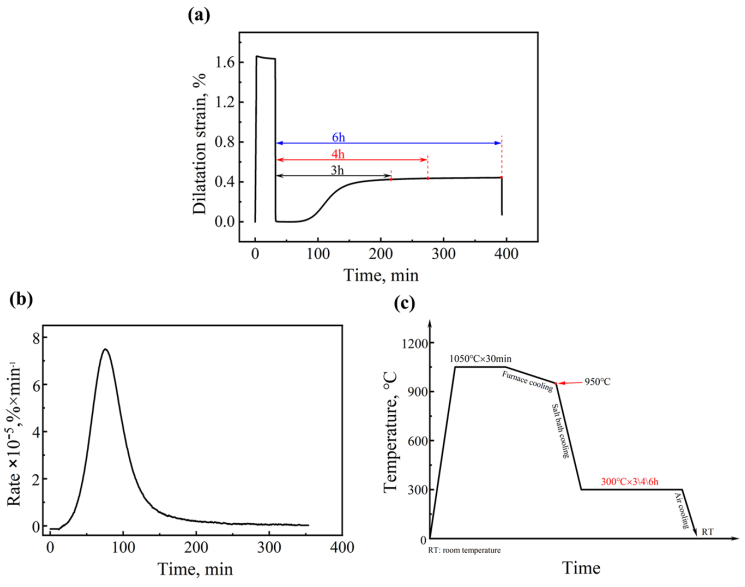


Figure 1. The curves of (**a**) dilatometric strain and (**b**) dilatometric strain rate austempered at 300 °C and (**c**) heat treatment process diagram.

Microstructural evolution was characterized by transmission electron microscopy (TEM), scanning electron microscopy (SEM), and X-ray diffraction (XRD). SEM was carried out using a Hitachi SU-5000 thermal field-emission SEM (Hitachi High-Technologies Corporation, Tokyo, Japan), and TEM was performed on an FEI Talos F200X equipped with a Super-X EDS system with four detectors (FEI Company, Hillsboro, OR, USA). TEM specimens were prepared by twin-jet electropolishing in a mixture of 92% glacial acetic acid and 8% perchloric acid. A Rigaku Smartlab-9KW diffractometer (Rigaku Corporation, Tokyo, Japan) with Co $K_{\alpha 1}$ radiation was employed for X-ray diffraction (XRD) analysis, using Co $K_{\alpha 1}$ radiation (λ = 1.789 Å) in the 1D mode, employing a scan rate of 1°/min and a step size of 0.01°/step, with a voltage of 40 kV and current of 135 mA. All XRD data were corrected for instrumental broadening and systematic deviations using annealed high-purity monocrystalline silicon powder, with the measurement conditions kept identical to those for the experimental steel. This allowed the determination of phase constituents, relative phase fractions, and carbon concentrations in austenite and ferrite, as well as dislocation density. To ensure a strain-free surface, the specimen underwent repeated polishing and etching cycles. The RA fraction (V_γ) was derived from Equation (1) [28], while the carbon content in RA (X_γ) was obtained from Equation (2) [29]. For enhanced accuracy, each XRD dataset was measured at least twice and subjected to multiple fitting iterations.

$$V_\gamma = \frac{(1/n_\gamma)\sum_{j=1}^{n_\gamma} I_\gamma^j / R_\gamma^j}{(1/n_\gamma)\sum_{j=1}^{n_\gamma} (I_\gamma^j / R_\gamma^j) + (1/n_\alpha)\sum_{j=1}^{n_\alpha} (I_\alpha^j / R_\alpha^j)} \quad (1)$$

$$a_\gamma \text{ (nm)} = (3.578 + 0.033C_\gamma)/10 \quad (2)$$

where n is the number of peaks examined, I is the integrated intensity, and R is the scattering factor, defined as $R = (1/v^2)\,[|F|^2 P((1 + \cos^2 2\theta)/\sin\theta\sin 2\theta)] \times e^{-2M}$, with v being the unit-cell volume, F the structure factor, P multiplicity factor, e^{-2M} the temperature factor, θ the diffraction angle, and a_γ(Å) the austenite lattice parameter.

The dislocation density was calculated using Equation (3) from the micro-strain broadening (ε) determined by Williamson–Hall analysis of the X-ray line profiles [30].

$$\rho = \frac{k}{F} \cdot \frac{\varepsilon^2}{b^2} \quad (3)$$

where for BCC metals k = 14.4, and the dislocation Burgers vector b (along <111>) has magnitude $b = \frac{\sqrt{2}}{2} a_\alpha$. For FCC metals, k = 16.1 with b along < 110 >, $b = \frac{\sqrt{3}}{2} a_\gamma$, where a_α and a_γ are the lattice parameters of ferrite and austenite, respectively, and F is taken as 1.

Room-temperature monotonic tensile tests were performed at a crosshead speed of 0.3 mm·min^{-1} on a universal testing machine (model E45.105) (MTS Systems Corporation, Eden Prairie, MN, USA), with strain measured by an Epsilon extensometer (25 mm gauge length) (Epsilon extensometer, Jackson, WY 83001, USA). Plate tensile specimens measured 110 × 30 × 2 mm, with the longitudinal axis parallel to the forging direction. Microhardness was measured using an FM-ARS 9000 tester (FUTURE-TECH CORP, Kanagawa 210-0804, Japan) under a load of 2.94 N. Tensile and microhardness tests were respectively conducted with three samples, and at least 2 repeated XRD scans were performed for each test status to improve the reliability, which provides sufficient parallel data to ensure the validity of the statistical results.

3. Results

3.1. Evolution of Microstructure with Prolonged Austempering Time

Typical SEM and TEM micrographs of the nanostructured bainitic steel austempered at 300 °C for 3 h, 4 h, and 6 h are presented in Figure 2. Upon completion of the nanostructured bainitic transformation after 3 h, no significant microstructural changes were observed with increasing austempering time. As shown in Figure 2f, no carbide precipitation is observed in the retained austenite of the 6 h specimen, which is attributed to the inhibiting effect of silicon atoms. Thus, all specimens exhibit a microstructure comprising BF, film-like RA (RA-F), and blocky RA (RA-B), where the blocky type is relatively coarse.

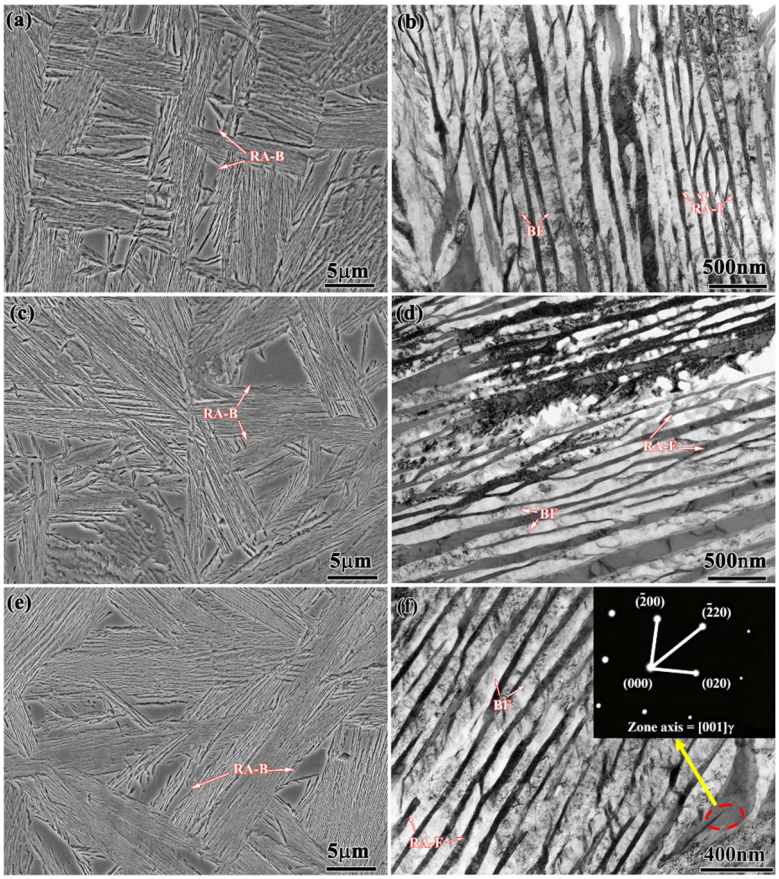


Figure 2. Typical SEM and TEM images of specimens austempered at 300 °C for various durations: 3 h (**a**,**b**); 4 h (**c**,**d**); and 6 h (**e**,**f**).

To further assess how prolonged austempering time influences the microstructure of nanostructured bainitic steel, Figure 3 illustrates the evolution of the average thickness of BF laths and RA. After the nanostructured bainitic transformation is completed at 300 °C for 3 h, prolonged austempering results in stable average thicknesses of approximately 54.0 nm for BF, 26.4 nm for film-like RA, and 1.14 μm for blocky RA. Thus, prolonging the austempering beyond the cessation of transformation does not significantly alter the dimensions or morphology of the constituent phases. The 3 h specimen, which is also representative of the 4 h and 6 h ones, was used to analyze the size distribution of blocky RA. The equivalent diameter of blocky RA in the 3 h specimen is $\leq$3 μm, with a substantial fraction measuring $\leq$2 μm, as shown in Figure 4, while those $\geq$2 μm represent only 10%.

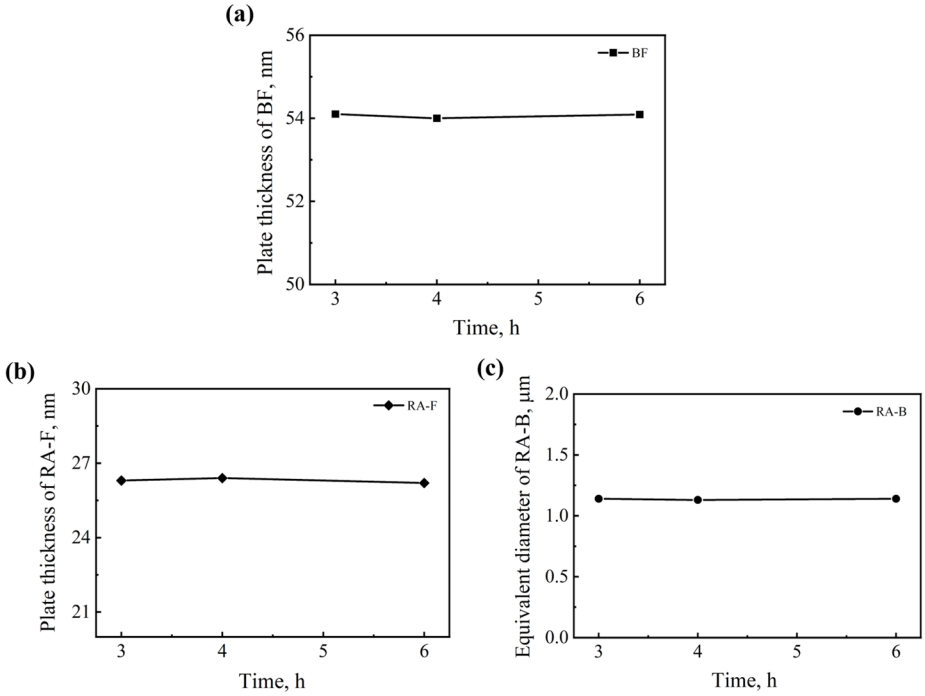


Figure 3. The average equivalent size with increasing austempering time. (**a**) BF; (**b**) RA-F. (**c**) RA-B.

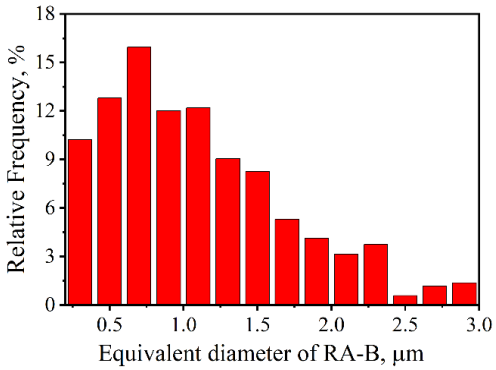


Figure 4. Equivalent diameter distribution of RA-B austempered at 300 °C with 3 h.

The XRD patterns of the 3 h, 4 h, and 6 h specimens are presented in Figure 5, revealing that all three microstructures consist of ferrite (α) and austenite (γ), which correspond to BF and RA, respectively. The $(200)_\alpha$ diffraction peak gradually decreases in its full width at half maximum (FWHM) with increasing austempering time, whereas its diffraction angle shows no significant change (Figure 5b). In contrast, the $(200)_\gamma$ peak gradually shifts leftward with prolonged austempering time (Figure 5c). This indicates that prolonged austempering reduces the micro-strain within the BF without altering its carbon content, while simultaneously increasing the carbon content of the RA during transformation stasis.

Quantified by peak fitting using Jade software (MDI Jade 6), the volume fraction of RA remains at 42.4 vol.% during prolonged austempering within transformation stasis. Furthermore, as illustrated in Figure 6, the RA in the 3 h, 4 h, and 6 h specimens is sufficiently stable to resist martensitic transformation during cooling to ambient temperature. That is, once the nanostructured bainitic transformation is complete, no further transformation of the RA occurs during prolonging austempering. Meanwhile, the RA exhibits a gradual increase in its average carbon content, rising from 1.77 wt.% (3 h) to 1.85 wt.% (6 h). Since the average carbon contents of RA-B and RA-F differ significantly (the former being lower),

their lattice constants show obvious differences; thus, the volume fractions and carbon contents were estimated by Gaussian multi-peak fitting [31,32], as shown in Figure 7.

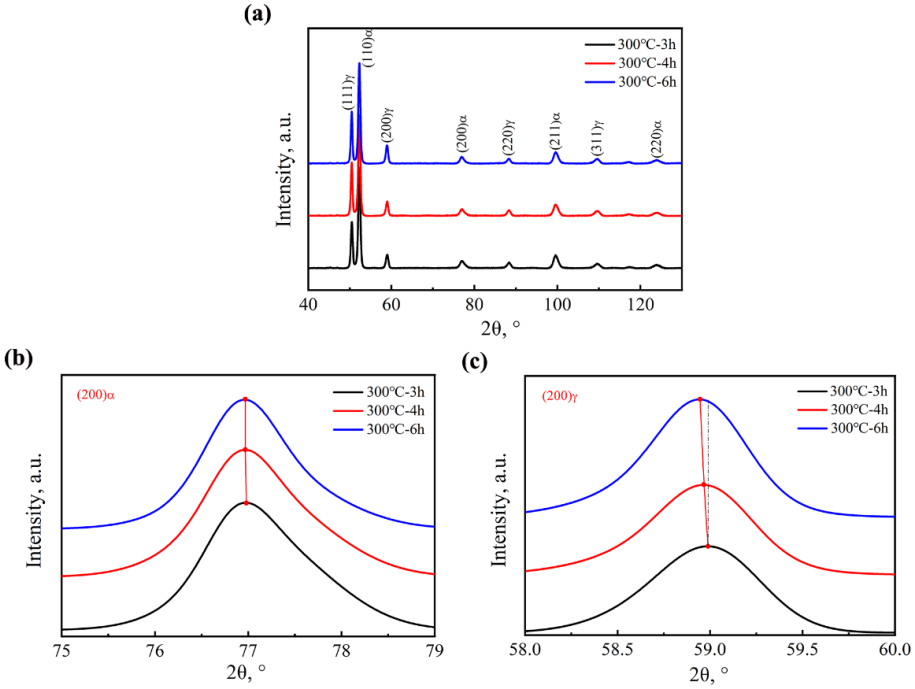


Figure 5. The XRD patterns of specimens austempered at 300 °C for various durations: (**a**) integrated patterns and (**b**,**c**) partial patterns.

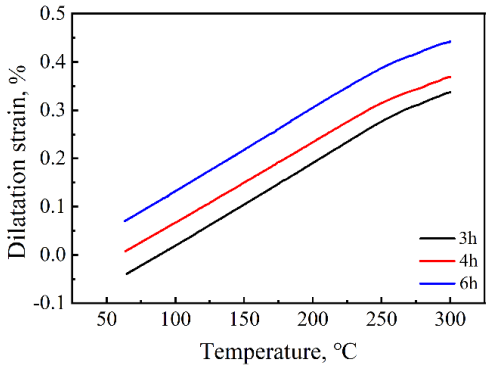


Figure 6. The dilatometric curves of specimens cooled to room temperature after bainitic transformation at 300 °C with various time.

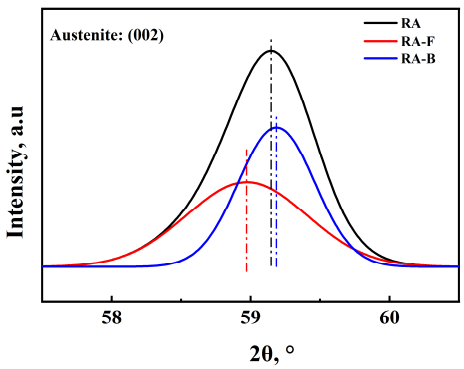


Figure 7. Schematic diagram of Gaussian multi-peak fitting for the (002) austenite peak.

In the fitting, the non-overlapping low-angle $(200)_\gamma$ peak of austenite was selected and fitted with a Gaussian function. Background treatment was performed automatically with Jade software. The initial peak positions were set at 59° for RA-B and 57.8° for RA-F. The actual fitting results showed that variations in the peak positions did not affect the final results; specifically, RA-B could vary within 59–59.5°, and RA-F within 58.5–59°, while the calculated volume fractions and carbon contents remained identical, confirming the high stability and robustness of the method.

The weighted average of deconvoluted sub-phase carbon contents cannot perfectly match the integral XRD bulk carbon value, due to two unavoidable experimental deviations: (1) a tiny volume fraction of transitional thin-sheet RA exists between film and blocky morphologies, which cannot be fully separated during Gaussian peak fitting and is not counted in $(V_b + V_f)$; (2) minor overlapping of ferrite and austenite diffraction backgrounds introduces small fitting errors in both integral and split-peak calculations. As shown in Table 1, upon prolonging the austempering time after the nanostructured bainitic transformation completes, the volume fractions of both blocky and film-like RA remained unchanged. However, the carbon content in both morphological types of RA increased with prolongation of the austempering time.

Table 1. The phase parameters of the RA and BF.

Time	V_γ (%)	C_γ (wt. %)	$V_{\gamma b}$ (%)	$C_{\gamma b}$ (wt. %)	$V_{\gamma f}$(%)	$C_{\gamma f}$ (wt. %)	ε_{micro} ($\times 10^{-3}$)	ρ_α ($\times 10^{15}$ m^{-2})
3 h	42.4 ± 0.2	1.77 ± 0.03	27.6 ± 0.01	1.75 ± 0.01	14.8 ± 0.3	2.03 ± 0.01	4.41 ± 0.04	4.51 ± 0.01
4 h	42.6 ± 0.3	1.82 ± 0.02	27.9 ± 0.01	1.80 ± 0.01	14.7 ± 0.1	2.10 ± 0.01	4.22 ± 0.06	4.13 ± 0.01
6 h	43.4 ± 0.1	1.85 ± 0.01	28.2 ± 0.01	1.83 ± 0.01	15.2 ± 0.1	2.13 ± 0.01	3.96 ± 0.03	3.64 ± 0.02

Note: V_γ represents the volume fraction of RA; C_γ denotes its carbon content. $V_{\gamma b}$ and $C_{\gamma b}$ correspond to the volume fraction and carbon content of blocky RA, respectively, while $V_{\gamma f}$ and $C_{\gamma f}$ denote those of film-like RA. Additionally, ε_{micro} represents the micro-strain, and ρ_α denotes the dislocation density of BF.

The newly formed bainite undergoes autotempering during the bainitic transformation [33]. Given the relatively high austempering temperature (300 °C) in this study, longer austempering times lead to a lower dislocation density within the BF. Specifically, it is reduced from 4.51×10^{15} m^{-2} in the 3 h specimen to 3.64×10^{15} m^{-2} in the 6 h specimen (Table 1).

The above analysis indicates that, although no significant difference in microstructure is observed with prolonged austempering within bainitic transformation stasis, the RA is gradually enriched with carbon. Generally, a significant carbon concentration gradient develops within the blocky RA after the completion of the nanostructured bainitic transformation [34], with the carbon content near the phase boundary being higher than that in the central region. Prolonging austempering promotes the diffusion of carbon atoms from phase boundaries into the blocky RA interior, resulting in overall carbon homogenization. Meanwhile, during prolonged austempering, the gradual recovery of dislocations in the BF releases carbon atoms originally segregated at dislocations, which subsequently diffuse into the adjacent RA, compensating for the reduction in carbon content at the austenite boundaries, and the characteristic time for carbon diffusion in ferrite and austenite is obtained from the following equation [35]:

$$t = l^2/6D \quad (4)$$

where t is the characteristic carbon diffusion time, l is the mean diffusion distance, taken as the half-width of the BF laths or that of the austenite blocks, and D is the diffusion

coefficient, which follows the Arrhenius relation $D = D_0\exp(-Q/RT)$, with D_0 being a constant ($D_{0\alpha} = 0.62 \times 10^{-6}$ m^2/s, $D_{0\gamma} = 0.10 \times 10^{-4}$ m^2/s). The activation energies Q are 80.4 kJ/mol (α) and 135.7 kJ/mol (γ). R is the gas constant, and T is the absolute temperature, following common convention.

Calculations show that carbon atoms diffuse from BF into the adjacent RA in just 0.04 s, indicating extremely rapid kinetics. As shown in Figure 8, the carbon diffusion distance in austenite for the 3 h specimen is 500 nm. Theoretically, this indicates that carbon homogenization is achieved in all film-like RA and in blocky RA with an equivalent diameter up to 1 μm, representing 50% of the total blocky RA. In the 4 h specimen, the carbon diffusion distance in austenite increases to 600 nm, and carbon homogenization is achieved in 63% of the blocky RA. Prolonging the austempering time to 6 h increases the diffusion distance to 750 nm, and achieves carbon homogenization in over 80% of the blocky RA. Concurrently, the overall carbon concentration gradient within the blocky retained austenite decreases significantly. Furthermore, the high dislocation density in the nanostructured bainite provides diffusion pathways for carbon atoms, thereby accelerating carbon diffusion [36,37]. Collectively, the above calculations and analyses indicate that the overall carbon distribution in RA will be significantly homogenized during austempering at 300 °C.

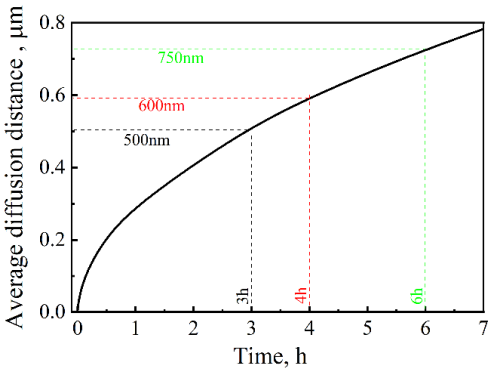


Figure 8. The curve of diffusion distance of carbon atoms in RA with increasing time.

3.2. Evolution of Mechanical Properties with Prolonged Austempering Time

Based on the above-mentioned results, the microstructure morphology of the nanostructured bainitic steel shows no significant changes during prolonged austempering within transformation stasis. However, a gradual recovery of dislocations is observed, along with increased carbon content in the RA and homogenized carbon distribution within it. Given that mechanical properties are governed by microstructure, the observed microstructural evolution is anticipated to affect its mechanical behavior.

Figure 9 presents the microhardness evolution with prolonged austempering time. A decrease in microhardness is observed from 552 HV for the 3 h specimen to 530 HV for the 4 h specimen. The microhardness remains essentially unchanged upon further prolongation to 6 h. This slight reduction in microhardness is ascribed to the decrease in dislocation density during prolonged austempering within transformation stasis.

Figure 10 shows the engineering stress–strain curves, true stress–strain curves, and work-hardening rate curves for the 3 h, 4 h, and 6 h specimens. Table 2 summarizes the corresponding mechanical properties. Following the bainite transformation, all specimens with different austempering times exhibit linear hardening after yielding, accompanied by a low work-hardening rate. The 3 h specimen exhibits continuous work hardening without plastic instability, whereas a certain degree of plastic instability is observed in the 4 h and 6 h specimens (Figure 10a).

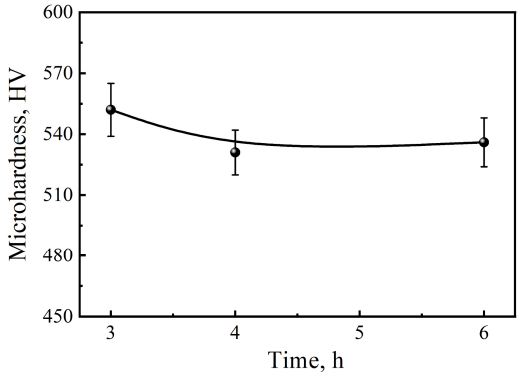


Figure 9. The microhardness of specimens with increasing austempering time.

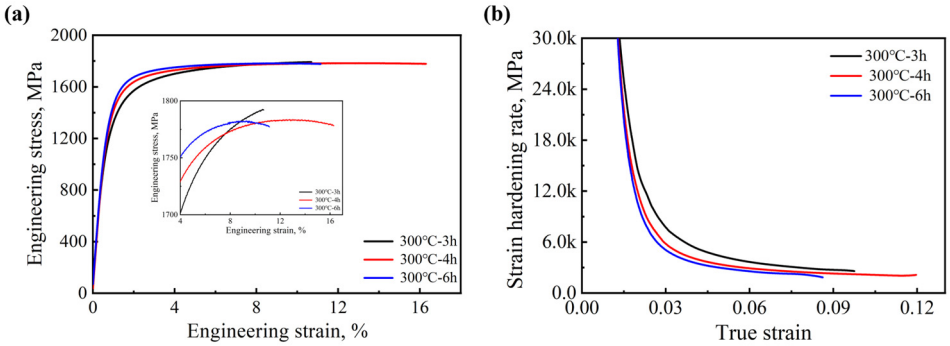


Figure 10. (**a**) Engineering stress–strain, and (**b**) strain-hardening rate curves.

Table 2. Mechanical properties of specimens austempered at 300 °C for various durations.

Time	Microhardness /HV	Yield Strength /MPa	Tensile Strength /MPa	Elongation /%	Uniform Elongation /%	PSE/GPa·%
3 h	552 ± 13	1308 ± 7	1792 ± 8	10.1 ± 1.9	10.1 ± 1.9	18.1 ± 0.8
4 h	531 ± 11	1335 ± 5	1782 ± 6	16.8 ± 1.1	11.5 ± 1.0	29.9 ± 0.5
6 h	536 ± 12	1374 ± 10	1781 ± 6	11.0 ± 0.1	9.5 ± 0.6	19.6 ± 0.2

Once the bainitic transformation completes, the nanostructured bainitic steel exhibits a higher yield strength with prolonged austempering time, increasing from 1308 MPa (3 h specimen) to 1374 MPa (6 h specimen). The ultimate tensile strength remains essentially unchanged, with values stabilized at approximately 1790 MPa (Table 2). Correspondingly, the work-hardening capacity gradually decreases with prolonged austempering time, primarily owing to the decreased dislocation density (Figure 10b). With prolonged austempering time, its total elongation shows a trend of first rising and then falling, peaking at 16.8% in the 4 h specimen. This specimen also has the highest uniform elongation of 11.5%. The product of strength and elongation (PSE), representing the energy absorbed prior to tensile failure, indicates the overall mechanical properties. Compared with the 3 h specimen where just the bainitic transformation completes, prolonged austempering enhances the PSE, as revealed by the comprehensive analysis. A maximum PSE of 29.9 GPa·% is attained in the 4 h specimen, representing a 65% increase over the 3 h specimen. Therefore, these results demonstrate the significance of prolonged austempering time within bainitic transformation stasis for the nanostructured bainitic steel.

3.3. Evolution of Mechanical Stability of RA with Prolonged Austempering

In the nanostructured bainitic steel, the work-hardening capacity and crack propagation resistance are closely linked to total elongation [38–40]. RA, a key phase within the nanostructured bainitic steel, accommodates deformation through mechanically induced martensitic transformation during plastic deformation. Its mechanical stability directly influences crack nucleation and crack propagation resistance [41]. After austempering at 300 °C is completed, microstructural evolutions during prolonged austempering time, such as carbon diffusion and dislocation recovery, influence the RA's mechanical stability, which in turn leads to variations in mechanical properties. The evolution of RA stability during tensile deformation was therefore investigated for specimens austempered at 300 °C for different times.

After tensile failure, XRD patterns were collected from two types of specimens: the undeformed ones and the fracture surfaces of the specimens austempered for 3 h, 4 h, and 6 h. These patterns are shown in Figure 11. The quantitative analysis using Jade software revealed that, on the tensile fracture surfaces, RA volume fractions for the 3 h, 4 h, and 6 h specimens are 27.3 vol.%, 13.6 vol.%, and 19.4 vol.%, respectively—significantly lower than the approximately 42.5 vol.% measured in the undeformed specimens. A comparison of the results reveals that, after the bainitic transformation is completed, prolonging the austempering time results in a higher proportion of RA that transforms via mechanically induced martensite during tensile deformation, thus affecting overall ductility in a differentiated manner.

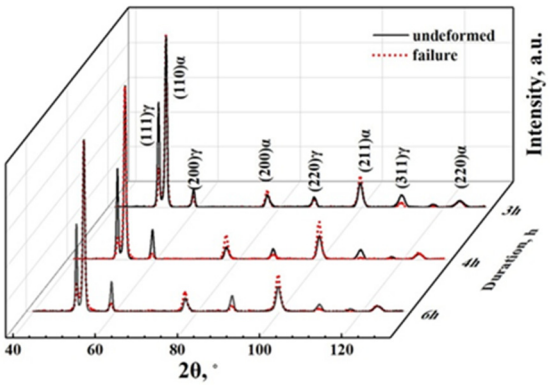


Figure 11. The XRD patterns of undeformed specimens and their tensile failure fracture austempered at 300 °C with various time.

To accurately reflect the RA content at different strain states during the interrupted tensile tests, XRD measurement locations were selected according to the following principles: (1) for specimens without necking, measurements were performed in the uniform deformation region; (2) for specimens that had necked but not fractured, measurements were performed in the necking region; (3) for fractured specimens, measurements were performed adjacent to the fracture surface. For each strain state, two parallel specimens were tested, and the measurement surface of each specimen was mechanically ground and polished to minimize errors arising from surface roughness and mechanical strain.

Figure 12 shows the evolution of RA volume fraction with engineering strain for the specimens austempered for 3 h, 4 h, and 6 h. In all cases, the fraction decreases with increasing strain, but this decline is markedly faster for the 4 h specimen than for the 3 h and 6 h ones. For the 3 h specimen, the RA volume fraction exhibits only marginal variation beyond an engineering strain of 8%, dropping from 28.2 vol.% at 8% strain to 27.3 vol.% at fracture (10.1%). This suggests that beyond 8% strain, the mechanically induced martensitic transformation of RA largely ceases during deformation. In the 4 h and 6 h specimens,

the RA volume fraction continuously decreases prior to necking, reaching 17.8 vol.% and 23.0 vol.%, respectively, at the maximum strain. Following the onset of necking, the RA volume fraction continues to decrease with further strain in both specimens. Notably, the reduction rate during this stage is higher for the 6 h specimen than for the 4 h specimen, which contrasts with the overall trend observed prior to necking.

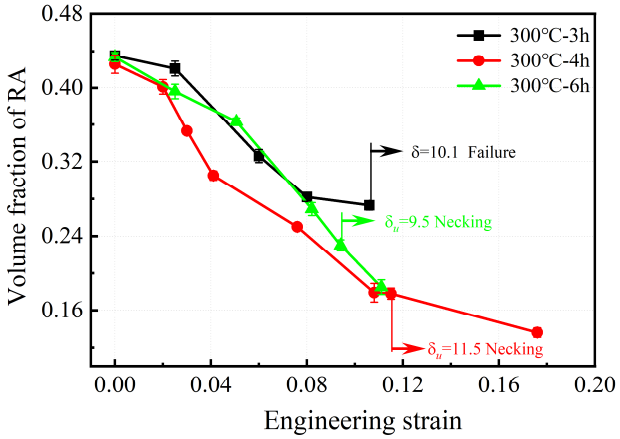


Figure 12. The volume fraction of RA in the specimens as a function of engineering strain.

Further characterization was performed on the evolution of RA's overall mechanical stability in the nanostructured bainitic steel after prolonged austempering at 300 °C. Figure 13 shows how the RA volume fraction (V) varies with true strain (ε) for the different specimens. The experimental data shown in Figure 11 were fitted using Equation (5) proposed by Sugimoto et al. [42].

$$V = V_0 exp(-k\varepsilon) \quad (5)$$

where V_0 and V are the RA volume fractions in the undeformed specimen and at true strain ε, respectively, and k is a constant quantifying the mechanical stability of RA, defined as its resistance to strain-induced martensitic transformation. A lower k value signifies greater resistance to transformation, and thus higher overall mechanical stability of the RA. The k values obtained from fitting are 4.71 (3 h specimen), 7.55 (4 h specimen), and 5.01 (6 h specimen). Thus, prolonging austempering after bainitic transformation at 300 °C initially lowers the mechanical stability of RA to its minimum at 4 h, followed by a mild increase at 6 h.

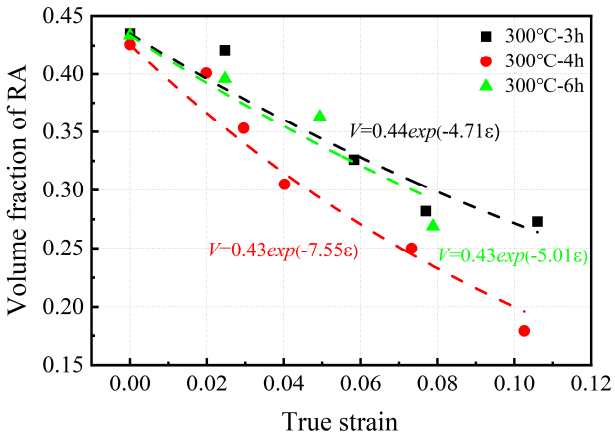


Figure 13. The fitting curves of the volume fraction of RA with increasing true strain in various specimens.

Compared with the 3 h specimen, the RA in the 4 h and 6 h specimens displays substantially lower mechanical stability. However, the 4 h specimen achieves 1.53 times the total elongation of the 6 h specimen, whose elongation is comparable to that of the 3 h specimen. This indicates that the contribution of RA to elongation is not solely governed by its stability. Previously, a similar reduction in RA stability was observed in the same steel after tempering at 380 °C [27]. Nevertheless, during tensile deformation, the RA underwent an abrupt transformation, producing untempered, hard, and brittle martensite. The substantial fraction of such untempered martensite limited the contribution of RA to the ductility. This indicates that the nanostructured bainitic steel's ductility also depends strongly on the rate at which RA undergoes mechanically induced martensitic transformation.

Figure 14 shows how the fraction and rate of RA transformation vary with true strain for the specimens austempered for 3 h, 4 h, and 6 h. During uniform deformation, all specimens exhibit a progressive increase in transformation fraction as true strain rises. Nevertheless, distinct trends are observed in the transformation rate among the different specimens. After the bainitic transformation completes, prolonging the austempering time significantly raises the initial transformation rate of RA during tensile deformation (Figure 14b). The transformation-rate of RA were obtained by taking the first-order derivative of the fitted curves of the retained-austenite volume fraction with respect to true strain (Figure 14a). The differentiation was performed using OriginPro 2021 software, following the menu sequence Analysis → Mathematics → Differentiate, with the derivative order set to 1.

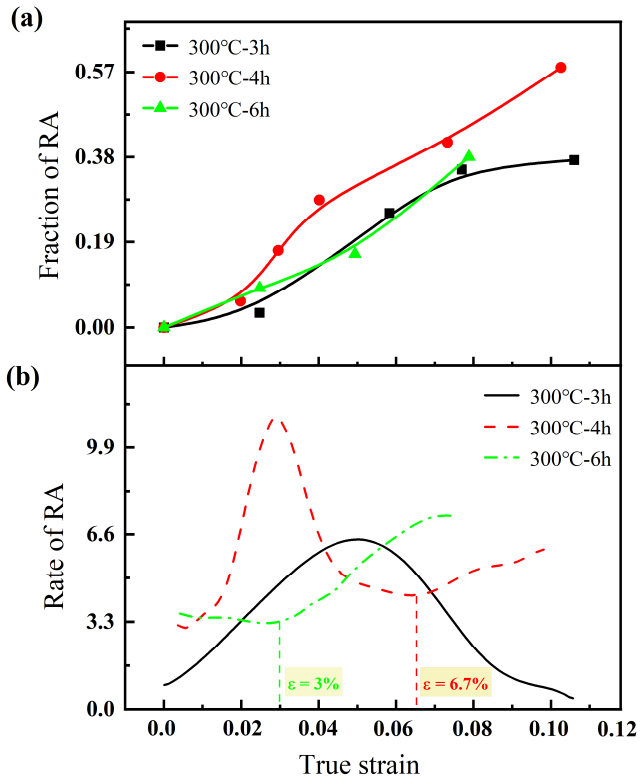


Figure 14. Variation in the (**a**) transformation fraction and (**b**) transformation rate of RA with true strain.

Further comparison reveals that the RA transformation rate in the 3 h specimen rises and then falls with strain, peaking at 5% true strain, whereas in the 4 h specimen it increases rapidly to a maximum at 3% true strain. With further strain, the transformation rate gradually decreases. When the true strain reaches 6.7% and beyond, the transformation

rate exhibits a slight increasing trend again. For the 6 h specimen, the mechanically induced martensitic transformation of RA proceeds at a relatively higher rate during the initial 0–3% true strain, with this rate remaining essentially constant. When the true strain exceeds 3%, the transformation rate in this specimen continuously increases. Therefore, prolonged austempering after bainitic transformation at 300 °C not only reduces RA's overall mechanical stability, but also significantly influences the rate of its mechanically induced martensitic transformation.

4. Discussion

4.1. Mechanism of Decreased Mechanical Stability of RA

Following completion of the bainitic transformation at 300 °C for 3 h, prolonged austempering does not significantly alter the RA size, morphology, or volume fraction, but its average carbon content progressively increases. Further comparative analysis shows that this holds for both blocky and film-like RA morphologies, with no decrease in carbon content in either case (Table 1). Therefore, from the perspective of its intrinsic characteristics, prolonged austempering after the bainitic transformation completes raises the critical stress required for strain-induced martensitic transformation, which improves its mechanical stability [43–45]. Nevertheless, the experimental results demonstrate that prolonged austempering reduces the RA's mechanical stability, albeit to varying degrees. RA's mechanical stability depends not only on its own state, including its size, carbon content, and morphology [46–48], but is also strongly affected by the surrounding bainitic ferrite, such as its strength, residual stress, and other factors [49–51]. Thus, it is evident that the surrounding bainitic ferrite matrix is the main factor responsible for the decrease in the stability of RA in this nanostructured bainitic steel, and a detailed analysis will be presented below.

Following the completion of the bainitic transformation at 300 °C for 3 h, prolonged austempering results in a decrease in the dislocation density within the BF, leading to a reduction in its strength. As a consequence, during tensile deformation, stress is more readily partitioned to the surrounding RA. Additionally, the annihilation of dislocations during prolonged austempering partially relieves the residual compressive stress within the nanostructured bainitic steel, and the work-hardening capacity of BF decreases accordingly [52,53], thus collectively accelerating the mechanically induced martensitic transformation of the RA. That is, prolonging the austempering after the bainitic transformation completes at 300 °C alters the BF matrix, promoting stress redistribution to RA and reducing the constraint on RA against mechanically induced martensitic transformation, which, overall, lowers the BF's shielding effect and consequently reduces the mechanical stability of RA in the 4 h and 6 h specimens. However, the 6 h specimen shows higher RA mechanical stability than the 4 h specimen, mainly due to its greater carbon content and faster initial transformation rate (Figure 14b), and the latter further confirms that stress partitioning to RA becomes more favorable with increasing austempering time. This rapid transformation leads to extensive stress-induced martensite, which accelerates failure and ultimately lowers the amount of transformed RA.

The above analysis demonstrates that prolonging austempering reduces RA's overall mechanical stability and significantly alters its transformation rate. In the 3 h specimen, increased deformation generates more martensite nucleation sites, accelerating the transformation under a higher mechanical driving force [54]. As strain increases, the growing fraction of transformed austenite refines the untransformed austenite and enriches its carbon content. Meanwhile, the high-strength BF matrix, with its substantial internal stress, cannot accommodate the volume expansion from transformation, increasing compressive stress on the RA. Collectively, these factors enhance the stability of the untransformed

austenite, causing its transformation rate to decline once true strain exceeds 5%. Prolonged austempering after the bainitic transformation weakens the shielding effect of BF on RA. This increases stress transfer to the austenite during initial tensile deformation, while auto-tempering reduces residual compressive stress and its hindrance to martensitic transformation. Consequently, the initial transformation rate of RA is accelerated in both the 4 h and 6 h specimens. Compared with the 3 h specimen, the 4 h specimen exhibits a higher transformation rate of RA during initial tensile deformation. Its rate continuously increases below 3% strain, peaking above the overall rates of the 3 h and 6 h specimens. The higher peak transformation rate of the 4 h specimen may arise from two effects of prolonged austempering: a locally increased carbon concentration gradient within the blocky RA and reduced strength of the BF [15,27].

Prolonging austempering to 6 h raises both the average carbon content and its distribution uniformity in RA. This reduces the variation in chemical driving force for strain-induced martensitic transformation, allowing more RA to transform under stress. Consequently, in the 6 h specimen, at strains below 3%, the RA transforms at a consistently high rate. Above 3% strain (corresponding to a true stress above 1784 MPa), the transformation rate progressively accelerates. This acceleration likely stems from the lower dislocation density in the BF of the 6 h specimen than in the 3 h and 4 h specimens. The reduced dislocation density leads to a diminished work-hardening capacity, enabling the BF to more readily accommodate the dilatational strain associated with martensitic transformation, thereby reducing its constraint on the transformation.

4.2. Strengthening and Toughening Mechanism

Based on the above findings, prolonging austempering after bainitic transformation completes lowers both the dislocation density and the mechanical stability of RA in the nanostructured bainitic steel, thus affecting its strength and toughness. The associated strengthening and toughening mechanisms are discussed in this section.

Two factors account for the increased yield strength of the nanostructured bainitic steel after prolonged austempering. First, in the 4 h and 6 h specimens, the accelerated strain-induced martensitic transformation of RA at the early stage of tension compensates for the strength loss due to dislocation recovery [21,27]. Second, prolonged austempering promotes carbon atom–dislocation interactions, forming carbon atom clusters that pin dislocations, thereby raising the critical stress for dislocation motion during tensile deformation and contributing to the observed yield strength increase [27,55].

Although prolonging austempering time to 4 h and 6 h reduces the mechanical stability of RA, thereby increasing martensite formation during plastic deformation, the work-hardening capacity progressively decreases. This decline stems from two factors: stress relaxation accompanying martensite formation offsets its hardening effect, and reduced dislocation density weakens dislocation interactions during deformation. These results confirm that dislocation density dominates work-hardening capability in the nanostructured bainitic steel. The combined effects on yield strength and work-hardening capacity during prolonged austempering thus leave the ultimate tensile strength essentially unchanged.

Prolonging the austempering time after the bainitic transformation at 300 °C significantly alters its elongation. To understand this effect on elongation, crack propagation at tensile fracture surfaces was investigated. Figure 15 shows longitudinal-section micrographs of the fracture surfaces of the 3 h, 4 h, and 6 h specimens. For the 3 h specimen, cracks initiate and propagate within coarse blocky RA, occasionally tearing along BF lath boundaries (Figure 15a). These short, straight crack paths reflect low energy absorption. The high-magnification analysis reveals that a few cracks propagate between BF laths, as well as nucleate and propagate at the interfaces between fine blocky RA and ferrite, with

blocky RA indicated by red arrows (Figure 15b). For the 4 h and 6 h specimens, cracks mainly nucleate and propagate within or along the boundaries of fine blocky RA, as well as across BF laths, with fine blocky RA marked by red arrows (Figure 15c–f). The 4 h specimen shows longer and more twisted crack paths than the 3 h specimen (Figure 15c), consistent with higher energy absorption. Higher magnification additionally reveals that some cracks also nucleate and propagate along coarse blocky RA boundaries and along the longitudinal direction of BF laths (Figure 15d). For the 6 h specimen, cracks similarly nucleate and propagate predominantly within or along the fine blocky RA boundaries, but the paths are relatively straight. Simultaneously, more cracks propagate along BF lath packets while fewer propagate across laths, indicating reduced crack propagation resistance and lower energy absorption (Figure 15e,f).

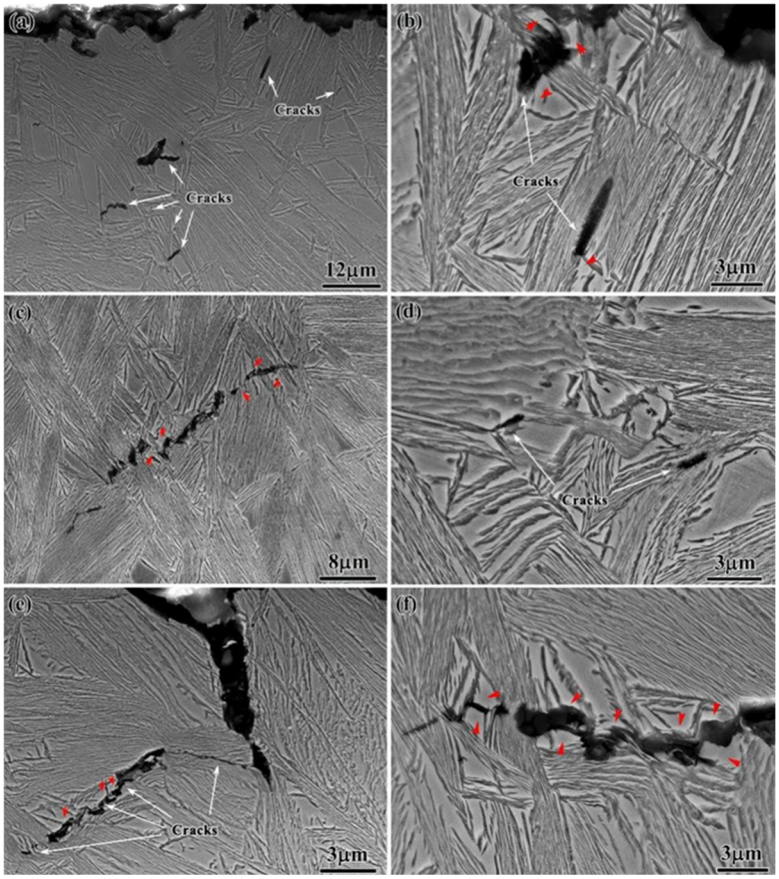


Figure 15. SEM images of microcrack at fracture of tensile failure specimen austempered at 300 °C for (**a**,**b**) 3 h; (**c**,**d**) 4 h; and (**e**,**f**) 6 h. Note: Red arrows indicate RA-B.

Comparison of crack initiation and propagation paths among the three specimens reveals distinct differences in their fracture modes. Generally, RA not only accommodates plastic deformation but also relieves stress concentration through its mechanically induced martensitic transformation, thereby enhancing the overall deformation compatibility of the nanostructured bainitic steel. After prolonged austempering within transformation stasis, the dislocation density of the matrix is only slightly reduced, with no significant change in its deformability. Based on the above analysis, the differences in elongation among the specimens austempered for different times are further elucidated below in conjunction with the evolution of the mechanical stability of RA. For the 3 h specimen, the RA possesses the highest mechanical stability, with its martensitic transformation ceasing once the strain reaches 8% or above. This prevents it from further accommodating stress concentration to coordinate deformation. As a result, under high stress concentration, cracks nucleate at

coarse blocky RA/martensite interfaces and propagate rapidly, leading to relatively poor overall plasticity.

In the 4 h and 6 h specimens, prolonged austempering significantly reduces the mechanical stability of RA, leading to more mechanically induced martensite formed during plastic deformation to relieve stress concentration. However, a marked difference in elongation is observed between the two specimens. In contrast to the 6 h specimen, the RA in the 4 h specimen undergoes continuous martensitic transformation at a relatively low rate once the strain exceeds 4%, thereby continuously enhancing deformation compatibility. However, at 11% strain, approximately 24.4 vol.% untempered hard and brittle martensite forms, accelerating crack initiation at fine blocky RA boundaries with higher mechanical stability and triggering plastic instability. Following instability onset, the RA in the 4 h specimen continues to transform at a low rate (Figure 12), continuing to accommodate deformation and potentially closing cracks, which increases crack propagation resistance. Moreover, more cracks propagate across BF laths, which may be associated with the transformation of film-like RA located between the laths. Synergistically, the continuous and stable transformation of RA and the crack propagation across BF laths ultimately account for the highest elongation observed in the 4 h specimen. For the 6 h specimen, the transformation rate of RA remains high and continuously accelerates once the strain exceeds 3%. The resulting extensive formation of hard and brittle martensite accelerates crack nucleation, leading to premature plastic instability. Furthermore, after instability onset, the RA continues transforming at a high rate (Figure 12), generating more hard and brittle martensite that accelerates crack propagation, and thus reduces total elongation. Thus, it is evident that the continuous and stable mechanically induced martensitic transformation of RA during tensile deformation underlies the optimal elongation of the 4 h specimen. This may be attributed to the moderate reduction in the strength of the bainitic ferrite laths and the locally elevated carbon concentration gradient near the interfaces of the blocky retained austenite in the 4 h specimen [15,27].

5. Conclusions and Prospects

This study systematically investigated the evolution of microstructure and mechanical stability of retained austenite (RA) in nanostructured bainitic GCr15Si1Mo steel, as well as their effects on mechanical properties, with a focus on the influence of prolonged austempering time (from 3 h to 4 h and 6 h). The main conclusions are drawn as follows:

(1) Prolonging the austempering time beyond the bainitic transformation at 300 °C (after 3 h) leaves the microstructure and RA volume fraction largely unchanged, but gradually increases the carbon content of RA—more in blocky than in film-like RA—while progressively reducing dislocation density. Together, these changes influence the mechanical stability of RA and the resulting strength–ductility balance.

(2) Prolonging austempering after bainitic transformation alters both RA's overall mechanical stability and the kinetics of its strain-induced martensitic transformation. As time goes on, the stability follows a non-monotonic trend: first a drop, then a rise. Yet for the 4 h and 6 h specimens, it remains below the 3 h level. Prolonged austempering also accelerates the initial transformation rate during tension and produces different rates at later stages. Among all the specimens, the 4 h specimen shows the most favorable, continuous, and stable transformation rate throughout deformation.

(3) After the bainitic transformation completes at 300 °C (3 h), prolonged austempering lowers the microhardness from 552 HV to 536 HV. The ultimate tensile strength stays around 1790 MPa, whereas yield strength rises from 1308 MPa to 1374 MPa. Influenced by both RA's mechanical stability and its strain-induced martensitic transformation rate, the total elongation shows a non-monotonic trend with austempering time: first

increasing, then decreasing. In this study, the 4 h specimen exhibited the highest total and uniform elongation among all specimens. Consequently, its strength-elongation product (PSE) reached a peak value of 29.9 GPa·%, which is 1.65 times that of the 3 h specimen.

The clarified regulation of retained austenite stability and the TRIP effect within transformation stasis provides a theoretical reference for factories to adjust continuous salt bath austempering production lines. Manufacturers can appropriately extend the holding time in a certain range to customize steels with matched plasticity according to different component forming requirements.

This work systematically reveals the evolution of the microstructure and mechanical properties of nanostructured bainitic bearing steel under prolonged austempering within transformation stasis, yet the present study has an obvious limitation in that all microstructural statistics rely solely on 2D electron microscopy characterization. Subsequent research will adopt AI-assisted 3D microstructure reconstruction technology to eliminate planar projection deviation, combine unified 2D/3D multi-scale microstructural descriptor models for bainitic steel, and adopt serial-Section 3D characterization to quantify the three-dimensional network evolution of retained austenite during tensile deformation [56–58]. The 3D topological evolution law of RA and its intrinsic correlation with the TRIP effect will be further clarified to realize more accurate prediction of strength–ductility synergy performance of nanostructured bainitic steel.

Author Contributions: X.W.: Conceptualization, methodology, validation, investigation, resources, data curation, writing—original draft preparation, writing—review and editing, visualization, funding acquisition; Y.W.: Conceptualization, formal analysis, resources, writing—review and editing, funding acquisition; D.S.: methodology; writing—original draft preparation; software; J.C.: validation, resources, project administration, funding acquisition; L.W.: software, validation, data curation; W.L.: software; formal analysis; writing—original draft preparation; C.L.: validation; formal analysis; writing—original draft preparation; Z.Y.: Conceptualization, formal analysis, investigation, resources, writing—review and editing, supervision, project administration, funding acquisition; F.Z.: Conceptualization, resources, supervision, funding acquisition; W.S.: writing—review and editing, funding acquisition. All authors have read and agreed to the published version of the manuscript.

Funding: The authors would like to thank the funding support for this work from the Shaanxi Natural Science Foundation (2025JC-YBQN-756), Hebei Province Special Project for Key Core Technology Breakthroughs in County-level Characteristic Industrial Clusters (26241026D), Advanced Materials-National Science and Technology Major Project (2025ZD0619502), Xi'an Talent Plan (XAYC240016), the National Natural Science Foundation of China (52307032), and the National Key R&D Program of China (2022YFE03150204).

Data Availability Statement: The original contributions presented in this study are included in the article. Further inquiries can be directed to the corresponding authors.

Conflicts of Interest: Xubiao Wang, Wei Liu and Cheng Liu were employed by the Xi'an QinChuang High Purity New Materials Technology Co., Ltd. The remaining authors declare that the research was conducted in the absence of any commercial or financial relationships that could be construed as a potential conflict of interest.

Appendix A

The appendix is a methodological framework figure that illustrates the research steps and methodology of this study to facilitate the reader's comprehension.

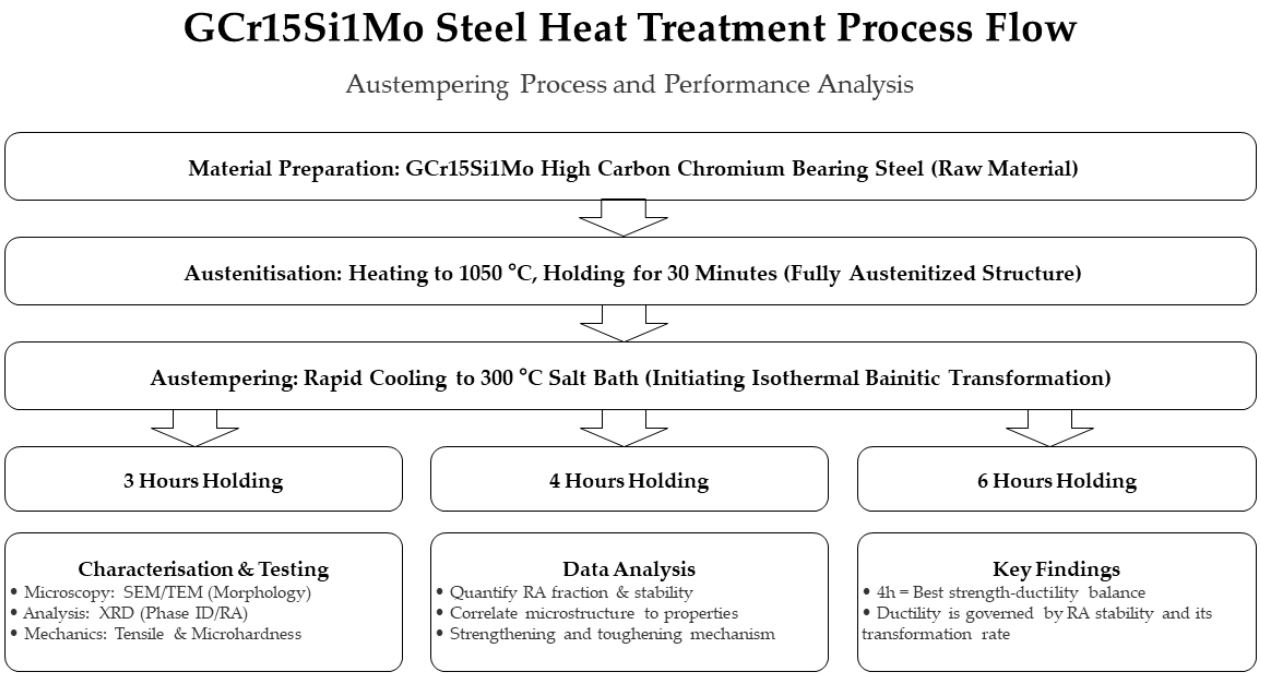


Figure A1. Methodological framework of this manuscript.

References

1. Morales-Rivas, L. Viewpoints on Technological Aspects of Advanced High-Strength Bainitic Steels. *Metals* **2022**, *12*, 195. [CrossRef]
2. Su, R.; Zheng, X.; Kang, J.; Wu, D.-Y.; Ma, H.-K.; Zhang, F.-C.; Yang, Z.-N.; Li, Q. Microstructure-property correlation and strain partitioning behavior in medium-carbon carbide-free bainitic steel. *J. Iron Steel Res. Int.* **2025**, *32*, 2039–2053. [CrossRef]
3. Wang, J.; Li, H.; Wang, Q.; Liang, Z.; Gao, S.; Sun, L.; Gao, X.; Yang, Z.; Li, Y.; Zhang, F. Effect of rapid tempering at high temperature on microstructure, mechanical properties and stability of retained austenite of medium carbon ultrafine bainitic steel. *J. Mater. Res. Technol.* **2024**, *28*, 3144–3154. [CrossRef]
4. Wang, Y.H.; Liu, Z.Q.; Wang, X.B.; Chen, X.; Zhang, X.; Shen, W.; Yang, Q.; Zhao, L.; Yang, Z. The effects of austempering time on mechanical properties of the novel GCr15Si1MoNbV bearing steel and on its rolling contact fatigue behaviors. *Int. J. Fatigue* **2026**, *207*, 109519. [CrossRef]
5. Shi, X.B.; Tu, X.Y.; Yan, B.C.; Ren, Y.; Yan, W.; Shan, Y.-Y. Effect of phase content on deformation compatibility in ferrite and bainite dual-phase steel: Experimental and crystal plasticity finite element analysis. *J. Iron Steel Res. Int.* **2025**, *32*, 743–755. [CrossRef]
6. Liu, Y.; Tian, J.; Liu, M.; Gan, X.-L.; Liu, S.; Xu, G. Effect of isothermal martensite and bainite transformation on microstructure and properties in a medium-carbon high-strength Q&P steel. *J. Iron Steel Res. Int.* **2024**, *31*, 3095–3108. [CrossRef]
7. Ingber, J.; Kunert, M. Prediction of the Martensite Start Temperature in High-Carbon Steels. *Steel. Res. Int.* **2022**, *93*, 2100576. [CrossRef]
8. Su, Y.; Yang, S.; Yu, X.F.; Zhou, C.; Liu, Y.; Feng, X.; Zhao, Q.; Wu, J. Effect of Austempering Temperature on Microstructure and Mechanical Properties of M50 Bearing Steel. *J. Mater. Res. Technol.* **2022**, *20*, 4576–4584. [CrossRef]
9. Kumar, A.; Blessto, B.; Singh, A. Effect of austempering temperature on high cycle fatigue behaviour in nanostructured bainitic steels. *Mater. Sci. Eng. A* **2022**, *846*, 143296. [CrossRef]
10. Wasiak, K.; Hinca, M.W.; Skołek, E.; Rożniatowski, K.; Wieczorek, A.; Świątnicki, W.A. Effect of austempering time on multiphase microstructure evolution and properties of carburized Cr-Mn-Si alloyed steel subjected to bainitization quenching & partitioning heat treatment. *J. Alloys Compd.* **2023**, *966*, 171489. [CrossRef]
11. Tanaka, S.; Shirahata, H.; Shigesato, G.; Takahashi, M. Carbon Enrichment of Austenite during Ferrite—Bainite Transformation in Low-alloy-steel. *ISIJ Int.* **2023**, *63*, 543–552. [CrossRef]
12. Xiao, B.; Yu, J.R.; Yu, Y.S.; Hu, B.; Misra, R.; Liu, S.; Liu, W. Uncovering the effect of retained austenite stability on the dynamic mechanical properties of TRIP-aided steel. *Mater. Sci. Eng. A* **2010**, *942*, 148729. [CrossRef]
13. Bhadeshia, H.K.D.H. Mechanism of the Bainite Transformation: A Turning Point. *Metall. Mater. Trans. A* **2025**, *57*, 1–20. [CrossRef]
14. Aalipour, Z.; Ghosh, S.; Kmi, J.; Javaheri, V. Effect of Partitioning Time and Silicon Content on Retained Austenite Stability in Medium-Carbon Advanced High-Strength Steels. *Procedia Struct. Integr.* **2025**, *69*, 105–112. [CrossRef]
15. Wang, X.B.; Liu, C.B.; Qin, Y.M.; Li, Y.; Yang, Z.; Long, X.; Wang, M.; Zhang, F. Effect of tempering temperature on microstructure and mechanical properties of nanostructured bainitic steel. *Mater. Sci. Eng. A* **2022**, *832*, 142357. [CrossRef]

16. Zhang, S.L.; Zhou, W.; Hu, F.; Yershov, S.; Wu, K. The role of Si in enhancing the stability of residual austenite and mechanical properties of a medium carbon bainitic steel. *J. Mater. Res. Technol.* **2024**, *30*, 1939–1949. [CrossRef]
17. Wang, K.; Gao, G.H.; Gui, X.L.; Bai, B.; Feng, C. Comparison of Microstructure and Mechanical Properties of a High-Carbon Bainitic Steel Treated by Long-Time Bainitic Austempering and Short-Time Austempering Plus Tempering Processes. *Steel Res. Int.* **2024**, *95*, 2300501. [CrossRef]
18. Gulbay, O.; Gramlich, A.; Krupp, U. Impact Toughness and Fatigue Crack Propagation in Carbide-Free Bainite: The Adverse Role of Retained Austenite and Martensite-Austenite Islands. *Fatigue Fract. Eng. Mater. Struct.* **2025**, *48*, 4217–4227. [CrossRef]
19. Jiang, T.; Liu, W.M.; Wei, S.Z.; Xu, L.; Yu, H.; Chen, C.; Diao, X.; Zhang, L.; Zhang, L.; Wang, R. Effect of tempering-induced microstructural evolution on the impact abrasive wear behavior of carbide-free bainitic steel: The crucial role of retained austenite stability. *Tribol. Int.* **2026**, *219*, 111838. [CrossRef]
20. Hu, L.; Zha, J.; Zhao, W.H.; Peng, X.-F.; Chen, Y.-L. Multi-dimensional controllability analysis of precision ball bearing integrity. *Adv. Manuf.* **2023**, *11*, 682–693. [CrossRef]
21. Zhao, J.L.; Zhang, F.C.; Lv, B.; Yang, Z.; Chen, C.; Long, X.; Zhao, X.; Chu, C. Inconsistent effects of austempering time within transformation stasis on monotonic and cyclic deformation behaviors of an ultrahigh silicon carbide-free nanobainite steel. *Mater. Sci. Eng. A* **2019**, *751*, 80–89. [CrossRef]
22. Hofer, C.; Winkelhofer, F.; Clemens, H.; Primig, S. Morphology change of retained austenite during austempering of carbide-free bainitic steel. *Mater. Sci. Eng. A* **2016**, *664*, 236–246. [CrossRef]
23. Shakeri, B.; Heidari, E.; Boutorabi, S.M.A. Effect of Isothermal Heat Treatment Time on the Microstructure and Properties of 4.3% Al Austempered Ductile Iron. *Int. J. Met.* **2023**, *17*, 3005–3018. [CrossRef]
24. Long, X.Y.; Sun, D.Y.; Wang, K.; Zhang, F.; Yang, Z.; Li, Y.; Zheng, C. Effect of carbon distribution range in mixed bainite/martensite/retained austenite microstructure on mechanical properties. *J. Mater. Res. Technol.* **2022**, *17*, 898–912. [CrossRef]
25. Ribamar, G.G.; Escobar, J.D.; Kwiatkowski da Silva, A.; Schell, N.; Ávila, J.; Nishikawa, A.; Oliveira, J.; Goldenstein, H. Austenite carbon enrichment and decomposition during quenching and tempering of high silicon high carbon bearing steel. *Acta. Mater.* **2023**, *247*, 118742. [CrossRef]
26. Liu, M.; Xu, G.; Zhou, M.X.; Tian, J.; Yuan, Q. Effect of isothermal temperature and holding time on phase transformation and properties of super bainitic steel Fe-0.4C-2.2Mn-1.5Si. *J. Wuhan Univ. Sci. Technol.* **2017**, *40*, 345–350. [CrossRef]
27. Wang, X.B.; Zhang, X.Z.; Fang, Q.W.; Ma, H.; Zhang, R.; Liu, F.; Yang, Z.; Zhang, F. Effect of tempering on stability of retained austenite and tensile properties of nanostructured bainitic steel. *Mater. Sci. Eng. A* **2022**, *856*, 143958. [CrossRef]
28. Wang, Y.H.; Yang, Z.N.; Zhang, F.C.; Qin, Y.; Wang, X.; Lv, B. Microstructures and properties of a novel carburizing nanobainitic bearing steel. *Mater. Sci. Eng. A* **2020**, *777*, 139086. [CrossRef]
29. Wang, Y.H.; Yang, Z.N.; Zhang, F.C.; Wu, D. Microstructures and mechanical properties of surface and center of carburizing 23Cr2Ni2Si1Mo steel subjected to low-temperature austempering. *Mater. Sci. Eng. A* **2016**, *670*, 166–177. [CrossRef]
30. Wu, S.S.; Kou, Z.D.; Lai, Q.Q.; Lan, S.; Katnagallu, S.S.; Hahn, H.; Taheriniya, S.; Wilde, G.; Gleiter, H.; Feng, T. Dislocation exhaustion and ultra-hardening of nanograined metals by phase transformation at grain boundaries. *Nat. Commun.* **2022**, *13*, 5468. [CrossRef] [PubMed]
31. Huang, X.D.; Huang, Q.Y.; Jiang, Y.H.; Li, Z.; Shan, Q. Retained austenite stability in cementite-free bainitic steels processed by different isothermal heat treatments: Insights from quasi-in situ strain partition analysis. *Mater. Charact.* **2025**, *229*, 115474. [CrossRef]
32. Chen, M.J.; Hou, T.P.; Cheng, S.; Hu, F.; Yu, T.; Pan, X.; Li, Y.; Wu, K. A Comprehensive Exploration of the Relationship between Microstructure Optimization and Strength Enhancement in Low-Density 5Al-5Mn Steel. *Acta. Metall. Sin. Engl.* **2025**, *38*, 1219–1236. [CrossRef]
33. Tolouei, E.; Hurel, V.; Loucif, A.; Morin, J.-B.; Jahazi, M. Influence of the as quenched state and tempering temperature on the final microstructure and hardness of a high strength medium carbon steel. *Mater. Chem. Phys.* **2024**, *325*, 129765. [CrossRef]
34. Fan, S.C.; Guo, D.; Xu, Z.Q.; Hao, H.; Bai, Y.; Wei, L.; Dai, Y. Construction of multi-scale blocky retained austenite in nanostructured bainitic steel via two-step austempering. *Mater. Sci. Eng. A* **2025**, *924*, 147806. [CrossRef]
35. Gao, G.H.; Zhang, H.; Gui, X.L.; Tan, Z.; Bai, B.; Weng, Y. Enhanced strain hardening capacity in a lean alloy steel treated by a "disturbed" bainitic austempering process. *Acta. Mater.* **2015**, *101*, 31–39. [CrossRef]
36. Lin, S.; Borgenstam, A.; Stark, A.; Hedström, P. Effect of Si on bainitic transformation kinetics in steels explained by carbon partitioning, carbide formation, dislocation densities, and thermodynamic conditions. *Mater. Charact.* **2022**, *185*, 111774. [CrossRef]
37. Dong, B.Q.; Hou, T.P.; Wu, K.M.; Rolfe, B.; Kong, L.; Cai, M.; Hodgson, P. Microstructure features and carbon partitioning in low temperature bainitic steels: The effect of magnetic field. *Mater. Charact.* **2023**, *196*, 112635. [CrossRef]
38. Gupta, S.K.; Manna, R.; Chattopadhyay, K. Ductilization of high carbon, high silicon carbide-free nanostructured bainitic steel. *Mater. Sci. Eng. A* **2022**, *860*, 144318. [CrossRef]

39. Li, K.F.; Qian, L.H.; Wei, C.Z.; Yu, W.; Ding, Y.; Ren, L.; Chen, Z.; Zhang, F.; Meng, J. Study on the relationship between the microstructure characteristics, tensile properties and impact toughness of carbide-free bainitic steel. *Mater. Charact.* **2024**, *212*, 113991. [CrossRef]
40. Królicka, A.; Lesiuk, G.; Kuziak, R.; Radwański, K.; Janik, A. The Role of Microstructure Morphology on Fracture Mechanisms of Continuously Cooled Bainitic Steel Designed for Rails Application. *Metall. Mater. Trans. A* **2023**, *54*, 487–504. [CrossRef]
41. Zhang, T.Y.; Wang, Y.; Zhang, C.; Wang, L.; Di, H.; Xu, W. High cycle fatigue properties and fatigue crack propagation behavior of a bainite railway axle steel. *Int. J. Fatigue* **2023**, *172*, 107641. [CrossRef]
42. Kozłowska, A.; Radwański, K.; Matus, K.; Samek, L.; Grajcar, A. Mechanical stability of retained austenite in aluminum-containing medium-Mn steel deformed at different temperatures. *Arch. Civ. Mech. Eng.* **2021**, *21*, 19. [CrossRef]
43. Wang, K.; Gui, X.L.; Bai, B.Z.; Gao, G. Effect of tempering on the stability of retained austenite in carbide-free bainitic steel. *Mater. Sci. Eng. A* **2022**, *850*, 143525. [CrossRef]
44. Avishan, B.; Aghdam, M.C.; Khanmiri, M.H. Mechanical Stability of High-Carbon Retained Austenite and Corresponding TRIP Effect in Austempered Ductile Iron (ADI). *Int. J. Met.* **2025**, *20*, 462–472. [CrossRef]
45. Tolouei, E.; Saadati, M.; Morin, J.B.; Garcia-Mateo, C.; Jahazi, M. Influence of bainitic transformation temperature on microstructure evolution during isothermal holding and subsequent cooling. *Mater. Chem. Phys.* **2025**, *345*, 131248. [CrossRef]
46. Dong, X.X.; Shen, Y.F. Improving mechanical properties and corrosion resistance of 0.5 wt.% C TRIP steel by adjusting retained austenite stability and microstructural constituents. *Mater. Sci. Eng. A* **2022**, *852*, 143737. [CrossRef]
47. Tan, X.D.; Lu, W.J.; Rao, X. Effect of ultra-fast heating on microstructure and mechanical properties of cold-rolled low-carbon low-alloy Q&P steels with different austenitizing temperature. *Mater. Charact.* **2022**, *191*, 112086. [CrossRef]
48. Chai, Z.S.; Lu, Q.; Hu, J.; Wang, L.; Wang, Z.; Wang, J.; Xu, W. Effect of retained austenite on the fracture behavior of a novel press-hardened steel. *J. Mater. Sci. Technol.* **2023**, *135*, 34–45. [CrossRef]
49. Moon, J.; Bae, G.; Jeong, B.Y.; Shin, C.; Kwon, M.-J.; Kim, D.-I.; Choi, D.-J.; Lee, B.H.; Lee, C.-H.; Hong, H.-U.; et al. Ultrastrong and ductile steel welds achieved by fine interlocking microstructures with film-like retained austenite. *Nat. Commun.* **2024**, *15*, 1301. [CrossRef] [PubMed]
50. He, Y.S.; Zhou, H.Y.; Zhao, Y.C.; Zhang, T.; Liu, C.; Xu, L.; Shin, K.; Zheng, W. Investigating the thermal stability of compressive residual stress in a gradient nanostructured austenitic stainless steel by in-situ XRD and TEM. *Mater. Charact.* **2024**, *207*, 113610. [CrossRef]
51. Platl, J.; Bodner, S.; Leitner, H.; Turk, C.; Nielsen, M.-A.; Keckes, J.; Schnitzer, R. Local microstructural evolution and the role of residual stresses in the phase stability of a laser powder bed fused cold-work tool steel. *Mater. Charact.* **2022**, *193*, 112318. [CrossRef]
52. Gao, Z.H.; Gao, H.J.; Zhang, Y.D.; Wu, Q. Experiment and mechanism investigation on the effect of heat treatment on residual stress and mechanical properties of SiCp/Al–Cu–Mg composites. *Mater. Sci. Eng. A* **2023**, *884*, 145555. [CrossRef]
53. Bhuyan, D.; Sastry, G.V.S.; Patra, S.; Pradhan, S.; Manna, R. Effect of austempering time on bainite plate thickness and variant selection in a high carbon low alloy steel. *Mater. Charact.* **2023**, *200*, 112923. [CrossRef]
54. Ghahfarokhi, M.T.; Casoli, F.; Minnert, C.; Bruns, S.; Bruder, E.; Cabassi, R.; Durst, K.; Gutfleisch, O.; Albertini, F. Effects of nanoindents on the martensitic transformation of Ni-Mn-Ga shape-memory Heusler films: A study by high-resolution imaging as a function of temperature. *Acta Mater.* **2023**, *245*, 118603. [CrossRef]
55. Shamsujjoha, M. Evolution of microstructures, dislocation density and arrangement during deformation of low carbon lath martensitic steels. *Mater. Sci. Eng. A* **2020**, *776*, 139039. [CrossRef]
56. Uzun, F.; Korsunsky, A.M. Evolutionary artificial intelligence for 3D microstructure reconstruction based on inverse pole figure images. *J. Intell. Manuf.* **2025**. [CrossRef]
57. Nerella, D.K.; Jogi, T.; Gulbay, O.; Ali, M.A.; Shchyglo, O.; Steinbach, I. A 2D and 3D microstructural descriptor approach to bainitic steels: Insights from phase-field simulations. *Acta Mater.* **2026**, *314*, 122340. [CrossRef]
58. Chelladurai, I.; White, E.V.; Miles, M.P.; Homer, E.R.; Sachdev, A.K.; Fullwood, D.T. 3D Study of Microstructural Influences on Retained Austenite Transformation in Q&P 1180 Steel. *Crystals* **2025**, *15*, 1015. [CrossRef]

Disclaimer/Publisher's Note: The statements, opinions and data contained in all publications are solely those of the individual author(s) and contributor(s) and not of MDPI and/or the editor(s). MDPI and/or the editor(s) disclaim responsibility for any injury to people or property resulting from any ideas, methods, instructions or products referred to in the content.